

Microlensing as a possible probe of the internal structure of quasars

[Order TBD] Mihai Tomozeiu^{1,2}, Irshad Mohammed,¹ Manuel Rabold²,
Prasenjit Saha,¹ and Joachim Wambsgans³

¹*Physik-Institut, University of Zurich, Winterthurerstrasse 190, 8057 Zurich, Switzerland*

²*Institute for Computational Science, University of Zurich, Winterthurerstrasse 190, 8057 Zurich, Switzerland*

³*Zentrum für Astronomie der Universität Heidelberg, Mönchhofstrasse 12–14, 69120 Heidelberg, Germany*

7 July 2015

ABSTRACT

In quasars that have been lensed by galaxies, the point-like images sometimes show sharp brightness variations (microlensing). These brightness changes are associated with the innermost region of the quasar passing behind a complicated pattern of caustics due to the stars in the lensing galaxy. In this paper, we study whether the universal properties of optical caustics could enable extraction of shape information about the central engine of quasars. We present a toy model with a crescent-shaped source crossing a fold caustic. The silhouette of a black hole over an accretion disk tends to produce roughly crescent sources. When a crescent source crosses a fold caustic, the resulting light curve is noticeably different from the case of a disc or Gaussian source. The crescent parameters, apart from one degeneracy, can be recovered.

Key words: Supermassive black holes, microlensing, quasars.

1 INTRODUCTION

More than half a century after their discovery, quasars still maintain the interest of a productive part of the astrophysical community. Although several mechanisms have been proposed to explain how such systems function, a single mechanism is widely accepted at the present time. The model was first proposed by Salpeter (1964), followed by Zel’dovich & Novikov (1964) in the same year and Lynden-Bell (1969) five years later. The present name of the model is the Super-Massive Black Hole (SMBH) paradigm.

According to the paradigm, the object is powered through the accretion of matter from the proximal environment into the black hole. The radiation emitted excites the surrounding medium which becomes detectable as the narrow line regions, broad band regions and torus. Moreover, in the direction perpendicular to the accretion disk, where the medium is more transparent, jets will appear. When the medium between and observer and such an object is transparent a quasar can be observed (e.g., Begelman et al. 1984). In other words an active galactic nucleus (AGN) with one of the poles orientated towards Earth would be detected as a quasar by an observer.

Through extensive observations done in the past 50 years, an important part of the assumptions and details regarding the mechanism have been confirmed and uncovered. Still, the black hole shadow and the surrounding luminous accreting material (the black hole silhouette) remains to be probed. Advancements in the very long baseline interferometer observations have made possible since 2007, the detection of structures of a few Schwarzschild radii of Sgr A* at the center of our Galaxy (Doeleman 2008). Furthermore, jet launching structure near the supermasve black hole in M87 were resolved with the same observation tool (Doeleman et al. 2012). With all the advancement, the current number of baselines does not allow the direct generation of images from the observations still it does allow the fitting of the data to predefined models (Kamruddin & Dexter 2013).

A whole range of models have been applied starting from simple geometric models to more complex, physically sensible models ((Doeleman et al. 2008), (Broderick et al. 2011), (Mościbrodzka et al. 2009), (Dexter et al. 2010)). A significant fraction

of the later models predict a crescent shaped silhouette of the black hole. This motivated Kamruddin & Dexter (2013) to use a simple geometric crescent model to fit the data. The succesful results encouraged the authors to speculate that the shadow of the black hole will be observed in the near fututre with the previously mentioned observation method.

Hundreds of thousands of quasars have been detected up to date, mainly from the Sloan Digital Sky Survey. The great majority of them present a redshift larger than 2.15 of their spectra ((Pâris et al. 2014)). Therefore the typical distance to the objects is in the order of gigaparsecs or above. A value that is orders of magnitude larger than the distance to M87. Direct observation of the black hole silhouette of quasars require significant technological advances. We argue in the present paper that one can probe and study the black hole shadow and its proximal environment belonging to a quasar without having to resolve sub-event horizon scales. We consider that this is possible by analyzing the data from microlensing-events. Moreover, unlike with the few nearby AGNs, the study of the very large quasar population allows for the statistical refinement of the global properties of AGN by highlighting any particular characteristic that is present only in Sgr A* and M87 central region. Furthermore, the probing of the event-horizon-scale inner regions of a large number of objects will facilitate the study of the evolution of the previously mentioned region.

Gravitational microlensing of QSOs have been predicted as early as 1981 when Gott (1981) suggested that “if haloes of galaxies were composed of stars with masses less than $0.1 M_{\odot}$, then these stars acting as individual lenses whould produce fluctuations of the order of unity in the intensities of the QSO images on time scales of 1 -14 years ”. What creates the magnification event is the relative and independent motion of the lens and source with respect to the observer. Since the respective lens is surrounded by similar objects one would expect to observe during a long enough time interval multiple microlensing events of the same source, the QSO. The sequential alignment of the source and observer with different lensing objects will result in an aparently random increase of the QSO light flux analogous to the scintilation events in a meter of radioactivity.

Estimates of the Einstein radius for the particular case of a QSO at redshift 2 lensed by a compact stellar mass object at redshift 0.5 was found to be $10^{-6} \sqrt{M/M_{\odot}}$ arcsec (Wambsganss 2001). The Schwarzschild radius of the Sgr A* black hole, situated at 8 kpc from Earth (Reid 1993) spans an angle of 10 microarcsec on the sky (Doeleman 2008). If the quasars observed at $z = 2$ would have similar linear sizes, the aparent size of the luminous part of the QSO would be many orders of magnitude below the 1 microarcsec level. Therefore the aparent size would be significantly smaller than the corresponding Einstein radius of a solar mass lens. The magnitude differences between the Einstein angle and the aparrent size of the bright part of the QSO motivates the introduction in the first part of the paper of simplified models for calculating the lightcurves of QSO magnification events. The simplified models are introduced in the theory section of the present paper. The theory (II) section of the present article starts with an introduction to the basic microlensing theory in which we present the general microlensing equation followed by the concept of magnification. We underline that for the particular case of micro gravitational lensing, the images are not resolved and thus the magnifications of each images contribute to a total magnification. Furthermore, the concept of critical curves and caustics are introduced. Afterwards we focus on a particular catastrophe, namely the fold. We choose to study events related to the previously mentioned singularity since the magnification events caused by the crossing of such boundaries are most probable. A quick inspection of figure 1 by the reader should motivate the previous statement. In continuation we introduce the commonly used result involving the magnification of a point-like source near a fold singularity. Namely that the magnification is aproximately linear outside the caustic and decreases from infinity with the square root of the distance to the boundary when inside the caustic. In the last section of the theory (II) we present the general equations for estimating the flux received from an extended source near a fold. The only elements required to compute the flux as a function of time are the two dimensional brightness function of the object and the magnification of a point-like source. One of the core assumptions made when developing the simple models is that the Einstein angle is orders of magnitude greater than the apparent size of the source. Due to this assumption one can imagine the caustic as an infinite wall to be crossed by the source as presented in ???. The consequence of the limit is that the information regarding the profiles of the source along any direction parallel to the boundary value is reduced to the corresponding integral value. The effect allows the introduction of a one dimensional flux function, which is the two dimensional flux integrated along the axis paralel to the boundary. The one dimensional profile contains exhaustively all the information that can be extracted from the lens generated light-curve

In the third section we introduce the three source profiles used in our models and simulations. We start with two commonly used and simple sources. Namely the gaussian brightness distribution and the constant intensity disk. In addition we use a geometric crescent-shaped source effectively the same as the one introduced by (Kamruddin & Dexter 2013) with constant surface brightness.

The fourth section contains the results of our simplified models calculations, including the numerical equation for lightcurve calculations and the corresponding plots. In order to facilitate comparison bewteen the lightcurves of the three distinct sources, we constrain the luminosity and half-light radius of all sources to have the same value. Furthermore, towards the end of the section, the microlensing light curves were generated for more complex images of black hole silhouettes. Namely the images

of Sgr A* and M87 compiled in the paper (Ricarte & Dexter 2015) and based on simulations presented in (McKinney & Blandford 2009) article were used as sources.

We continue to the second part of the paper, where we have advanced the level of complexity of the amplification map. Using the Wambsganss gravitational lensing code (Wambsganss 1990) a realistic magnification map is generated. The numerical method, hierarchical tree structure and backwards raytracing, underlying the microlensing code is treated in section five. Aside from a basic review of the physical and numerical principles of the code, the description of its generalization from disk shaped source images to crescent ones can be found in the Microlensing code and magnification map as well. Furthermore, the mass distribution in the lens plane, chosen to produce the magnification map used in this analysis, is introduced and motivated.

In section 6, we carried out a likelihood analysis for the parameterisation of the different source shapes and study the degeneracies involved amongst them. To do so, we mocked the datasets corresponding to each source shape and contaminate them with different noise components. Finally we run MCMC to explore the parameter space of the source shape and some nuisance parameters. The motivation of this part is to explore the possibility if using a simple toy model is it possible to differentiate between symmetric and asymmetric sources based on maximum likelihood analysis.

Finally, in the Discussion (VII) section, the main results of the current work and their implications are discussed.

2 THEORY

2.1 Basic microlensing theory

We start by introducing in a succinct manner the gravitational lensing theory that is relevant for microlensing in general and for the scope of the present paper in particular. For a detailed presentation of the theory the reader is referred to the books and articles that represent the references of the current section (book by Schneider and others). The general microlensing equation can be written as:

$$\vec{y} = \begin{pmatrix} 1 - \gamma - k & 0 \\ 0 & 1 + \gamma - k \end{pmatrix} \vec{x} - \sum_{i=1}^n m_i \frac{\vec{x} - \vec{x}_i}{(\vec{x} - \vec{x}_i)^2}. \quad (1)$$

The equation is valid for a set of n point (Schwarzschild) lenses placed at coordinates \vec{x}_i . \vec{y} represents the coordinates in the source plane for the respective ray, while \vec{x} represents the coordinates in the lens plane. Furthermore, γ and k are the shear and surface mass density. For the lens mapping, a Jacobian can be defined:

$$A(\vec{x}) = \begin{pmatrix} \frac{\partial y_1}{\partial x_1} & \frac{\partial y_1}{\partial x_2} \\ \frac{\partial y_2}{\partial x_1} & \frac{\partial y_2}{\partial x_2} \end{pmatrix}. \quad (2)$$

The determinant of $A(\vec{x})$ is related to the local magnification factor through the equation:

$$\mu(\vec{x}) = \left| \frac{1}{\det(A(\vec{x}))} \right| \quad (3)$$

According to this equation, from an infinitesimally small source positioned at \vec{x} in the lens plane an observer will receive a flux $\mu(\vec{x})dF$ instead of the flux dF that would be observed in the absence of the gravitational lens. In other words the source will dim or brighten depending on whether $\mu(\vec{x})$ is subunitary or supraunitary.

In general, for a single infinitesimally small source more than one image can be observed, each with magnification μ_j . For microlensing events the angular sizes of the images cannot be resolved. The only observable is the flux to which all nearby images contribute. A total magnification

$$\mu_t = \sum_j \mu_j \quad (4)$$

can be defined and account for an increase/decrease of brightness from all images.

2.2 Magnification of a point source near a fold

The determinant of the Jacobian A can have both positive and negative values depending in which region it is computed. Such regions are well defined and separated by critical curves where the determinant vanishes. The lens equation maps the critical curves of the lens plane into caustics in the source plane. An example of the caustic shape can be seen in figure 1.

Along these critical curves in the lens plane or caustics in the source plane, the magnification μ is infinite, a result that simply follows from equation 3. This statement holds only for infinitesimally small sources. For extended sources the

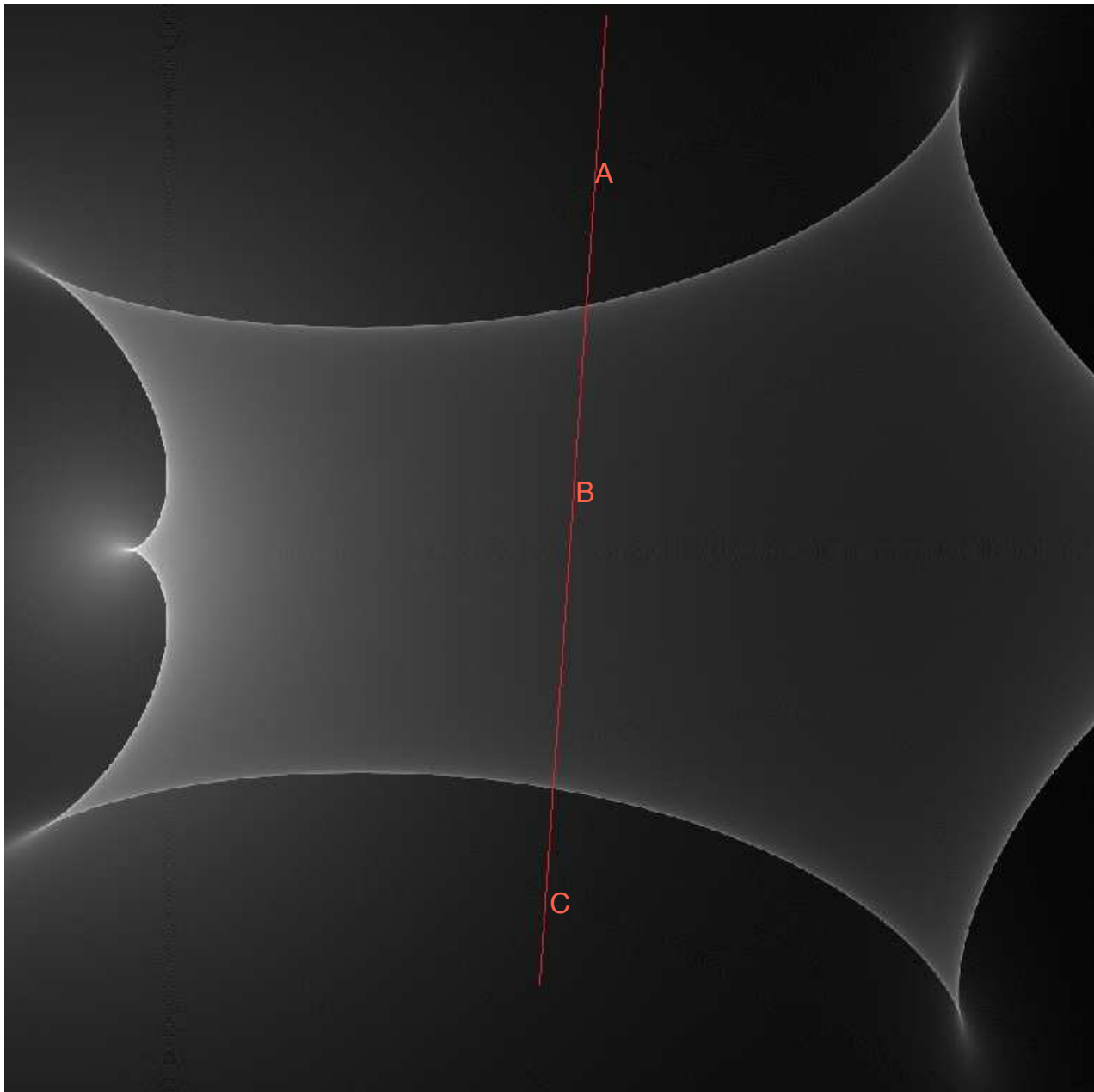


Figure 1. Magnification map

maximum amplification is finite since only an infinitesimally small area of the source overlaps with the caustics (Schneider & Weiss 1986).

The matrix A at the coordinates of the caustic can have rank 1 or 0. If the rank is 1 then the coordinates belong to *fold* or *cuspl* catastrophes. For the purpose of this paper we are interested only in the behaviour around *fold* catastrophe. A condition necessary to distinguish between a fold and cusp singularity is that the eigenvector of A corresponding to the null eigenvalue is not a tangent vector of the critical curve (Schneider & Weiss 1992)(Dominik 2008).

The behaviour of the images of a point source and their corresponding magnifications near such a caustic has been thoroughly studied in the past. The reader who is interested in understanding the details related to this subject is referred to papers such as Blandford & Narayan (1986), Schneider & Weiss (1992), Gaudi & Petters (2002a), Gaudi & Petters (2002b). For the present paper we only summarize the common result:

$$\mu_t(p) = \mu_0 + C_0 \frac{1}{\sqrt{p}} \Theta(p). \quad (5)$$

As the previous equation describes the magnification of a point source near a caustic is equal to the sum of the magnification due to other reasons μ_0 , assumed to be locally constant, and a decrease with the square root of the distance from the fold.

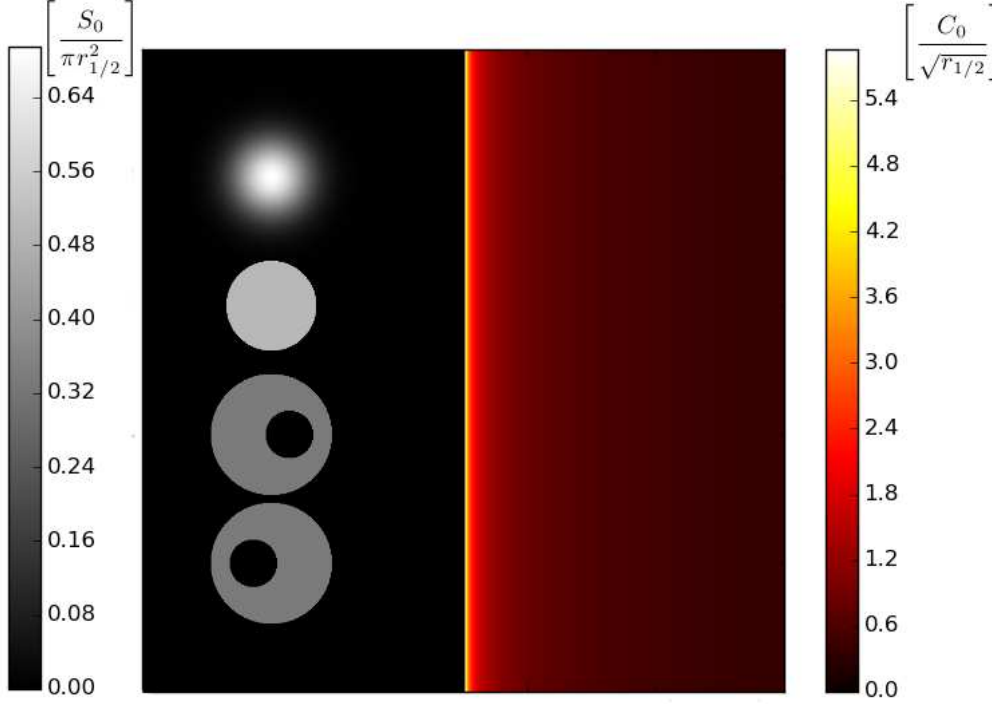


Figure 2. Source profiles for gaussian, disk, crescents (right) and magnification map for an infinite fold (left). Objects have the same S_0 and $r_{1/2}$.

The later term becomes activated only after the source enters the region interior to the caustic curves when the values of the stepfunction $\Theta(p)$ become unity. The proportionality constant C_0 is sensible only to the local behaviour of Fermat's potential and units used for the lens plane coordinates $\vec{q}(p, q)$.

2.3 Magnification of an extended source near a fold

A source of arbitrary shape can be described by a two dimensional brightness function $S_{2D}(p - p_s, q - q_s)$ defined for a coordinate system p, q where p_s, q_s denote the coordinates of the center of source.

For a microlensing event the lightcurve can be written for an undefined source shape as:

$$F(t) = \int_{-\infty}^{\infty} \int_{-\infty}^{\infty} S_{2D}(p - p_s(t), q - q_s(t)) \mu_t(p) dq dp \quad (6)$$

In order to build the previous equation we have considered that the time dependency of the flux F is given only by the motion of the source with respect to a fixed caustic. Therefore the only time dependent quantities in the right hand side of the equation are the coordinates of the center of the source p_s, q_s and by construct S_{2D} .

Due to the choice of the coordinate system the amplification factor has no dependence on the q coordinate. The previous equation can be rewritten as:

$$F(t) = \int_{-\infty}^{\infty} \mu_t(p) S_{1D}(p - p_s(t)) dp, \quad (7)$$

where we have defined the one dimensional flux function as:

$$S_{1D}(p - p_s(t)) = \int_{-\infty}^{\infty} S_{2D}(p - p_s(t), q - q_s(t)) dq \quad (8)$$

This representation is a valid approximation only when the apparent size of the source is much smaller than the corresponding Einstein angle of the lens. In this context all the information about the source shape and brightness that can be contained in the lightcurve is exhaustively given by the 1D flux function. In other words, if two sources with different S_{2D} have the same S_{1D} they cannot be distinguished by studying their lightcurves.

3 MODELS FOR EXTENDED SOURCES

In the present study we are analysing three types of sources with different surface brightness:

- (1) a rotationally symmetric source with a bivariate gaussian surface brightness distribution,
- (2) a disk source with constant surface brightness distribution,
- (3) a crescent shaped source with constant surface brightness distribution.

The first two sources are the typical choices used in the literature to describe the luminous parts of a quasar (Prasenjit should give some citations here). The third one is a recently proposed variant (Kamruddin & Dexter 2013).

3.1 Rotationally symmetric source with a bivariate gaussian surface brightness distribution

A symmetric 2D gaussian can be described mathematically as:

$$S_{2D}^G(p - p_s, q - q_s) = \frac{S_0^G}{2\pi\sigma^2} e^{-\frac{(p-p_s)^2}{2\sigma^2}} e^{-\frac{(q-q_s)^2}{2\sigma^2}}. \quad (9)$$

The corresponding 1D brightness is:

$$S_{1D}^G(p - p_s) = \frac{S_0^G}{\sqrt{2\pi}\sigma} e^{-\frac{(p-p_s)^2}{2\sigma^2}}. \quad (10)$$

Other parameters of the model are the total flux S_0^G and σ .

Although such a definition for a source would have non-zero surface/linear brightness for any coordinate p, q , the amount of light received by a detector from outside a 3σ disk centered at p_s, q_s would be insignificant. For a gaussian distributed surface brightness source the half-light radius is directly proportional to the parameter σ according to the equation:

$$r_{1/2} = \sqrt{\ln(4)}\sigma. \quad (11)$$

3.2 Disk source with constant surface brightness distribution

One can construct mathematically a disk source with constant surface brightness and radius R using a stepfunction:

$$S_{2D}^D(p - p_s, q - q_s) = \frac{S_0^D}{\pi R^2} \Theta(R^2 - (p - p_s)^2 - (q - q_s)^2). \quad (12)$$

By integrating over q coordinate the linear brightness function is obtained:

$$S_{1D}^D(p - p_s) = \frac{2S_0^D}{\pi R} \sqrt{1 - \frac{(p - p_s)^2}{R^2}} \Theta(R^2 - (p - p_s)^2). \quad (13)$$

The half-light radius of a uniform disk source is $R/\sqrt{2}$.

3.3 Crescent source with constant surface brightness distribution

The surface brightness distribution of a geometric crescent can be built by considering two disk sources of constant brightness. One larger disk will contribute positively to the total flux, while one smaller disk that is interior to the large one will contribute negatively. This superposition can be written for 2D as:

$$S_{2D}^C = S_{2D}^{Dp} - S_{2D}^{Dn}(n + 1) \quad (14)$$

with

$$S_{2D}^{Dp}(p - p_{sn}, q - q_{sn}) = \frac{S_0^{Dp}}{\pi R_p^2} \Theta(R_p^2 - (p - p_{sp})^2 - (q - q_{sp})^2) \quad (15)$$

and

$$S_{2D}^{Dn}(p - p_{sn}, q - q_{sn}) = \frac{S_0^{Dn}}{\pi R_n^2} \Theta(R_n^2 - (p - p_{sn})^2 - (q - q_{sn})^2). \quad (16)$$

The following notations were used: $R_p, (p_{sp}, q_{sp}), R_n, (p_{sn}, q_{sn})$ are the radii and coordinate of the center for the larger positive disk and smaller negative disk respectively. S_0^{Dp}, S_0^{Dn} represent the total flux of radiation received from the large and small disk. From this point forward we will not use the total flux from each source. Instead we will use the difference which in this case is the total flux from the crescent-shaped source S_0^C .

Equation 14 can be written as:

$$S_{2D}^C = \frac{S_0^C}{\pi (R_p^2 - R_n^2)} \left\{ \Theta [R_p^2 - (p - p_{sp})^2 - (q - q_{sp})^2] - \Theta [R_n^2 - (p - p_{sn})^2 - (q - q_{sn})^2] \right\}. \quad (17)$$

Analogous for the linear brightness function:

$$S_{1D}^C = \frac{2S_0^C}{\pi (R_p^2 - R_n^2)} \left\{ \sqrt{R_p^2 - (p - p_{sp})^2} \Theta [R_p^2 - (p - p_{sp})^2] - \sqrt{R_n^2 - (p - p_{sn})^2} \Theta [R_n^2 - (p - p_{sn})^2] \right\}. \quad (18)$$

There are some constraints on the parameters used to define a crescent in the previously presented manner that need to be stated. First, we must impose the obvious $R_p > R_n$ relation. Secondly, the small disk must always be interior to the large disk:

$$R_p \geq R_n + \sqrt{(p_{sp} - p_{sn})^2 + (q_{sp} - q_{sn})^2} \quad (19)$$

For the distances between the centers of the two disks we will use the same notations as the one found in the paper (Kamruddin & Dexter 2013), $a \equiv p_{sn} - p_{sp}$ and $b \equiv q_{sn} - q_{sp}$.

The half-light radius of any source is invariant to any rotational transformation. In the present case of a crescent source the effective radius is dependent on the parameters R_p, R_n and $\sqrt{a^2 + b^2} \equiv c$ exclusively. From symmetry considerations the centroid of the source is colinear with the centers of the two disks and it is situated at a distance d_c from the center of the bright disk. d_c can be computed numerically with the use of a variation of equation 18:

$$\frac{S_0^C}{2} = \frac{2S_0^C}{\pi (R_p^2 - R_n^2)} \int_{d_c}^{R_p} \left[\sqrt{R_p^2 - p^2} - \sqrt{R_p^2 - (p - c)^2} \Theta (R_p^2 - (p - c)^2) \right] dp. \quad (20)$$

With the position of the centroid determined, the half-light radius can be also be computed numerically:

$$\frac{S_0^C}{2} = \frac{2S_0^C}{\pi (R_p^2 - R_n^2)} \int_0^{r_{1/2}} [\Theta_2 - \Theta_1] p dp; \quad (21)$$

$$\Theta_1 = \left[\pi - \arccos \frac{R_p^2 + p^2 - d_c^2}{2R_p p} - \arccos \frac{R_p^2 - p^2 + d_c^2}{2R_p d_c} \right] \Theta (p - R_p + d_c); \quad (22)$$

$$\Theta_2 = \pi - \arccos \frac{p^2 + (c + d_c)^2 - R_n^2}{2p(c + d_c)} \Theta (p + R_n - d_c - c). \quad (23)$$

4 LIGHTCURVES OF THE EXTENDED SOURCES DURING FOLD CROSSING

Using equation 7 and the one-dimensional flux function presented in the previous section one can compute numerically the lightcurves of the three extended sources for the simplified infinite-wall-caustics model.

4.1 Lightcurve of the gaussian source

The amount of light received by an observer from a source with a gaussian distributed brightness with σ and total flux S_0^G in the absence of any gravitational lensing is:

$$F^G(t) = \int_{-\infty}^{\infty} \left(\mu_0 + \frac{C_0}{\sqrt{p}} \Theta(p) \right) \left(\frac{S_0^G}{\sqrt{2\pi}\sigma} e^{-\frac{(p - p_s(t))^2}{2\sigma^2}} \right) dp. \quad (24)$$

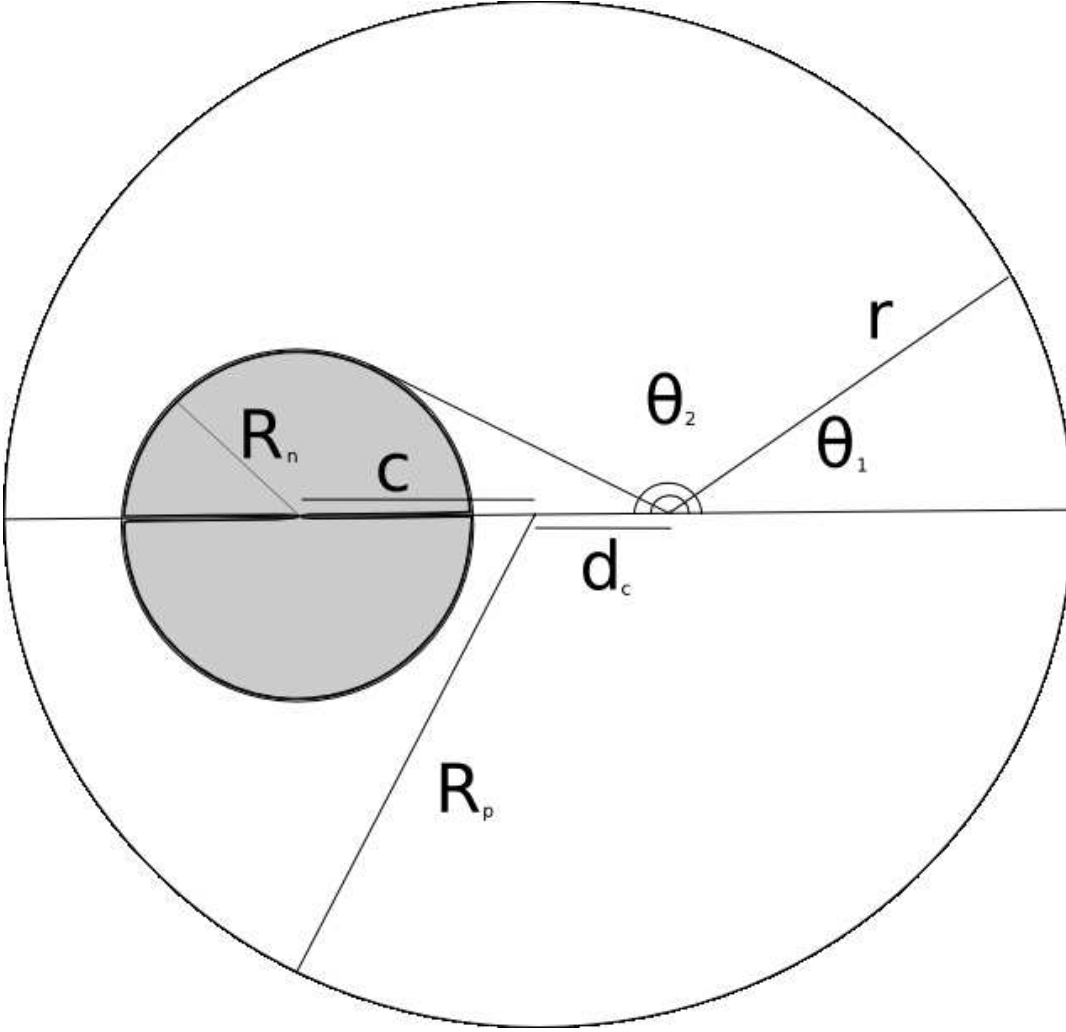


Figure 3. Geometry of crescent sources.

which can be simplified to:

$$F^G(t) = \mu_0 S_0^G + \frac{C_0 S_0^G}{\sqrt{2\pi}\sigma} \int_0^\infty \frac{e^{-\frac{(p-p_s(t))^2}{2\sigma^2}}}{\sqrt{p}} dp. \quad (25)$$

4.2 Lightcurve of the disk shaped source

Analogous to the gaussian shaped source, the disk source with uniform brightness, radius R and unmagnified flux S_0^D has a lightcurve described by the equation:

$$F^D(t) = \int_{-\infty}^\infty \left(\mu_0 + \frac{C_0}{\sqrt{p}} \Theta(p) \right) \left(\frac{2S_0^D}{\pi R} \sqrt{1 - \frac{(p-p_s(t))^2}{R^2}} \Theta(R^2 - (p-p_s(t))^2) \right) dp. \quad (26)$$

which is equivalent to:

$$F^D(t) = \mu_0 S_0^D + \frac{2C_0 S_0^D}{\pi R} \int_{\max(0, p_s(t)-R)}^{\max(0, p_s(t)+R)} \frac{1}{\sqrt{p}} \sqrt{1 - \frac{(p-p_s(t))^2}{R^2}} dp. \quad (27)$$

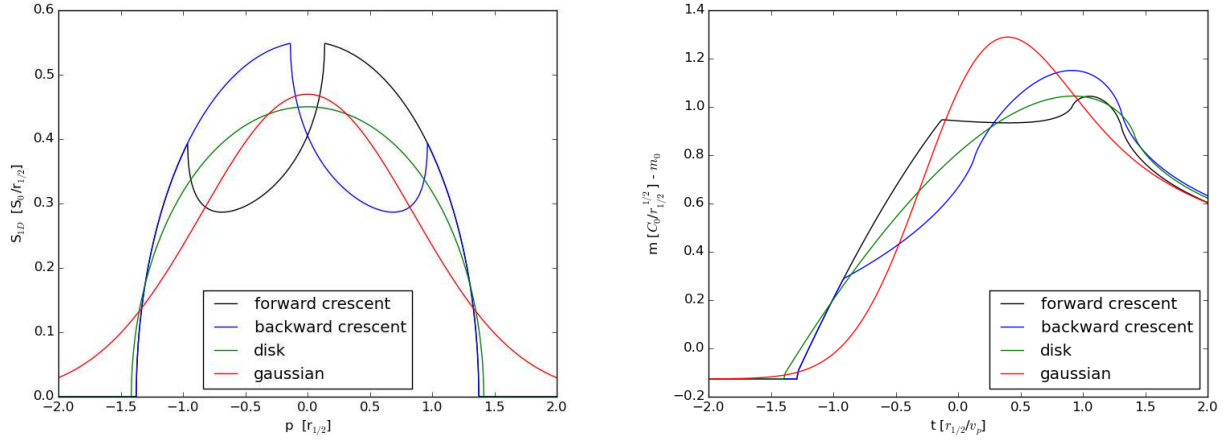


Figure 4. Lightcurves of crescents, gaussian and disk for sources with identical S_0 and $r_{1/2}$. Crescent source has $r_{1/2} = 0.72754 R_p$, $R_n = 0.4 R_p$, $a = 0.3/-0.3 R_p$

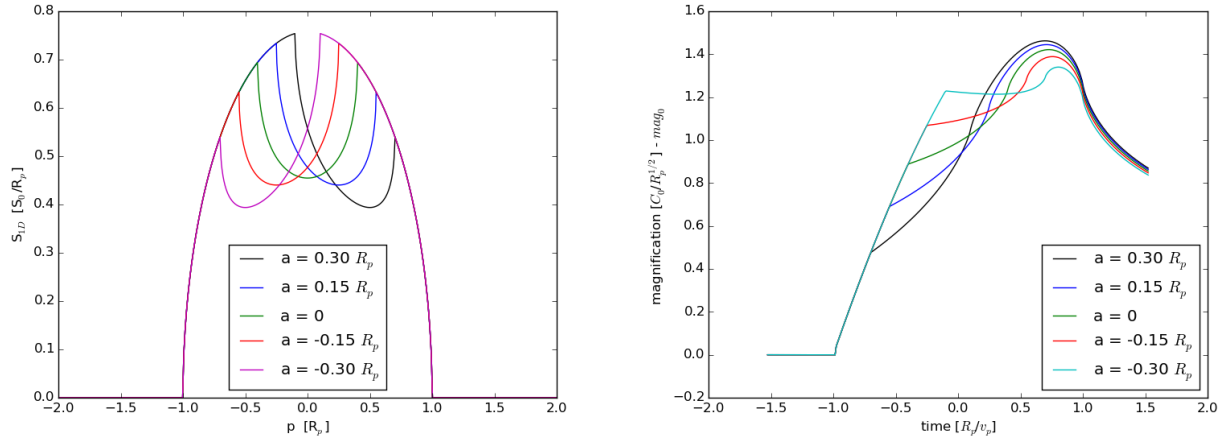


Figure 5. Lightcurves of crescent sources with $R_n = 0.4 R_p$.

4.3 Lightcurve of the crescent shaped source

The lightcurve of a crescent shaped source with unamplified flux S_0^C , radii R_p , R_n and center displacement $a(t)$ is:

$$F^c(t) = \mu_0 S_0^C + C_0 \frac{2S_0^C}{\pi(R_p^2 - R_n^2)} \left(\int_{\max(0, p_s(t)-R)}^{\max(0, p_s(t)+R)} \sqrt{\frac{R_p^2 - (p - p_s(t))^2}{p}} dp - \int_{\max(0, p_s(t)-a(t)-R)}^{\max(0, p_s(t)-a(t)+R)} \sqrt{\frac{R_p^2 - (p - p_s(t) + a(t))^2}{p}} dp \right) \quad (28)$$

The function $p_s(t)$ can be chosen to be equal to $v_p(t - t_0) + p_{s0}$. Where p_{s0} is the coordinate p of the source at the initial time, and v_p is the component of the velocity along the p axis. Such a modeling of the motion of the object in the source plane describes a linear motion with constant velocity. Furthermore, we reduce the complexity of the model by choosing the function $a(t)$ to be constant in time.

There are four characteristic points visible on the resulting one dimensional light profile of the crescent shaped source. Two of the points, p_1 and p_4 , mark the outer boundaries of the luminous disc component. The other two, p_2 and p_3 , mark the boundaries of the dark disc component. Since S_1D is a projection of S_2D on a line perpendicular to the caustic, the following relation holds:

$$p_2 - p_1 = R_p - R_n - a. \quad (29)$$

In addition there are two other obvious relations the characteristic points which are independent of the projection:

$$p_4 - p_1 = 2R_p, \quad (30)$$

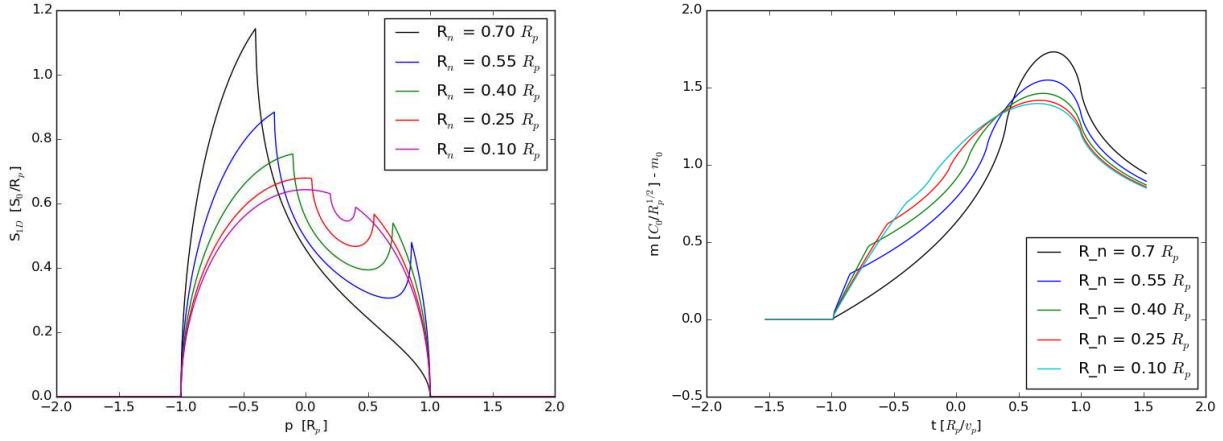


Figure 6. Lightcurves of backwards crescents with $a = 0.3 R_p$.

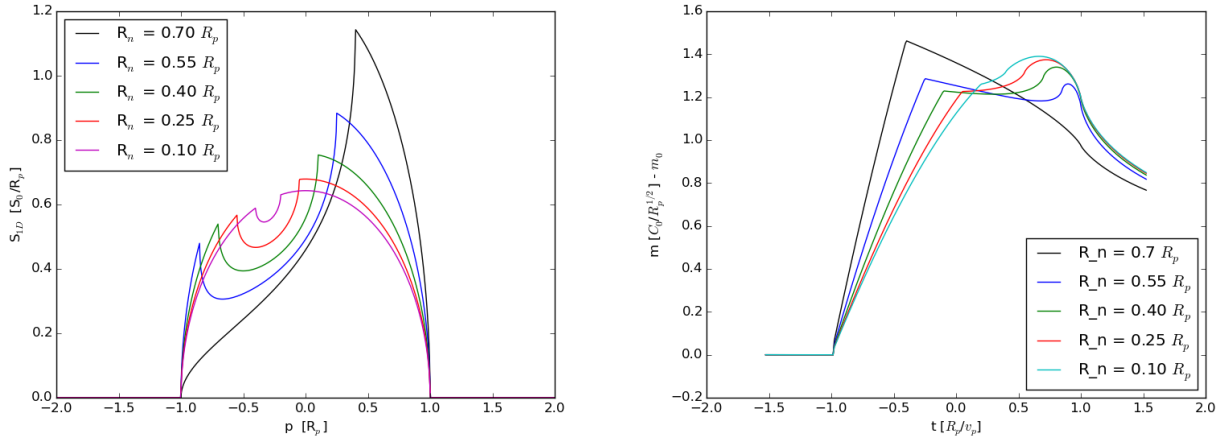


Figure 7. Lightcurve of forwards crescents with $a = -0.3 R_p$.

$$p_3 - p_2 = 2R_n. \quad (31)$$

All four points mark the positions where derivative $\frac{dS_{1D}}{dp}$ is discontinuous. The points can be used to define three regions: $p_1 - p_2$ where S_{1D} is convex, $p_2 - p_3$ where S_{1D} is concave, and $p_3 - p_4$ where S_{1D} is convex again.

Due to the nature of the caustic and the monotonic behaviour of the magnification map on both sides of the caustic. The previously mentioned characteristic points are inherited by the microlensing lightcurve. The points on the temporal dimension t_1, t_2, t_3 and t_4 correspond to instances in time when the fold is aligned with p_1, p_2, p_3 and p_4 , respectively. For a constant relative velocity v_p between the source and the caustic there is a simple relation between the points p_i and instances t_i :

$$t_j - t_i = \frac{p_j - p_i}{v_p}. \quad (32)$$

With the use of the previous four equations the following identities can be written:

$$R_p = \frac{v_p(t_4 - t_1)}{2}, \quad (33)$$

$$R_n = \frac{v_p(t_3 - t_2)}{2}, \quad (34)$$

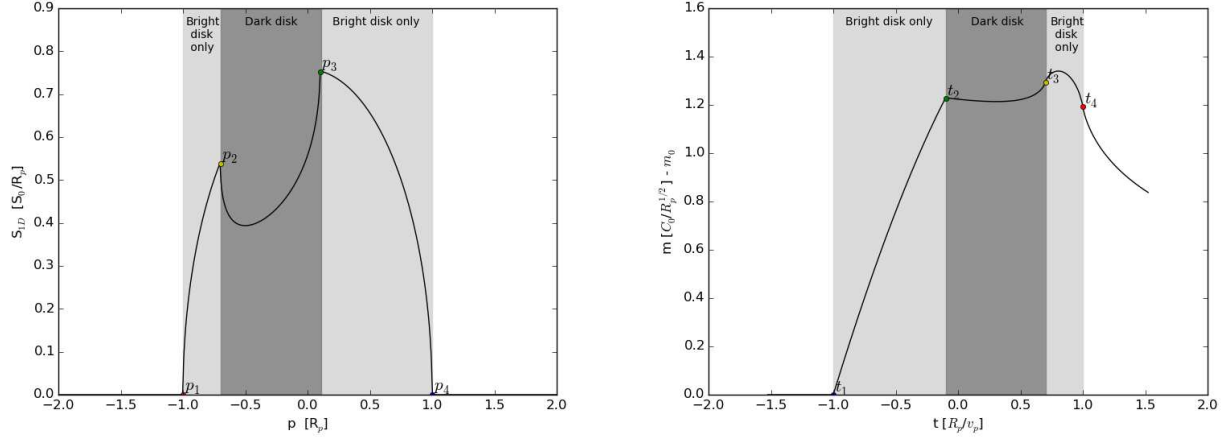


Figure 8. The characteristic points and instances of a crescent source’s one dimensional profile and microlensing lightcurve.

$$a = \frac{v_p (t_4 + t_1 - t_3 - t_2)}{2}. \quad (35)$$

Figure 4 reveals that the lightcurve of a crescent source has more visible features than the other two light-curves corresponding to the disc and gaussian shape. There are three regions where S_{1D} and by inheritance the lightcurve have distinguishable behaviour. The first region that would be recorded on a lightcurve plot represents the period of time when the bright disk begins to be overlapped by the caustic and stops when just before the dark disk reaches the caustic. During this period of time the flux of light from the source is increasingly magnified. The second period starts and ends with the overlapping of the dark disk. As a boundary of the two regions there is a distinguishable point where slope of the magnification is drastically changed. This apparent discontinuity in the first derivative of the magnification function is caused by the caustic amplification of the sudden drop in the S_{1d} function. During the respective period the magnification growth slows or even reverses during the first part of the period and starts to grow faster again as the dark disk ends its overlap with the caustic. At the point where the dark disk clears the caustic the growth of the magnification is infinite, which appears as a saddle point on the lightcurve. Next, the final period correspond to the case when the dark disk has cleared the caustic and the bright disk continues to overlap with the caustic. During this period the lightcurve reaches a peak that for most of the parameter space is global and for the rest of the parameter space local. At the end of the period the growth of the magnification is negative infinite. the respective point appears as a second saddle point on the lightcurve. Past this point the magnification of any finite source will decay in roughly the same manner.

The impact of parameter a on the shape of the lightcurve can be observed in figure 5 (a-var). Sources where the center of the dark disk reaches the caustic before the center of the bright disk are characterized by a smoother broad peak in contrast to the cases where the center of the dark disk reaches the caustic after the bright disk. In the case of the latter the instance when the dark disk reaches the caustic corresponds to larger and larger magnifications until it becomes a local and even global peak. The effect of the R_n parameter on the lightcurve is presented in figures 6 and 7. For the particular set of parameters where $R_p = R_n + a$ the third period of time discussed previously does not exist. Particularizing further, if the value of the radius of the dark disk is comparable to the value of the radius of the bright one then the position and shape of the maximum magnification are strikingly different. In case the crescent reaches the caustic with the bright region first, the peak magnification happens when the dark region reaches the caustic and it is characterized by a sharp variation in magnification growth, In the opposite case the peak appears before the end of the bright disk reaches the caustic and shape is smoother.

4.4 Microlensing a simulated image of M87

(Dexter et al. 2012) have created a radiative image of M87 based on the GRMHD simulations presented in (McKinney & Blandford 2009). The respective image, reproduced in figure 9, has been projected to a 1D profile associated to the perpendicular direction to a fold caustic approaching the image from the right. The projection is presented in the left panel of figure 10. The amplification values of the flux of light corresponding to a microlensing event are presented in the right panel of figure 10. In general the behaviour of the lightcurve is similar to the geometric crescent source with the caveat that the

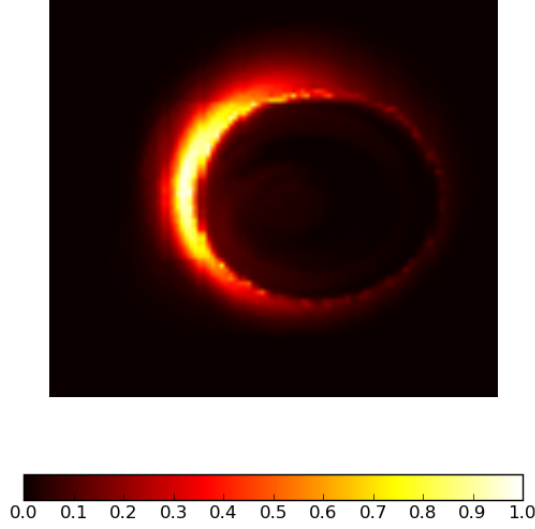


Figure 9. The simulated image of M87's black hole silhouette obtained by (Dexter et al. 2012) from a GRMHD simulation presented in (McKinney & Blandford 2009). The color bar is linear and scaled to reach value 1 for the maximum brightness. Points p_2 and p_3 , mark the start and end of the equivalent dark disk and are associated to the moment of their overlap with the caustic t_2 and t_3 .

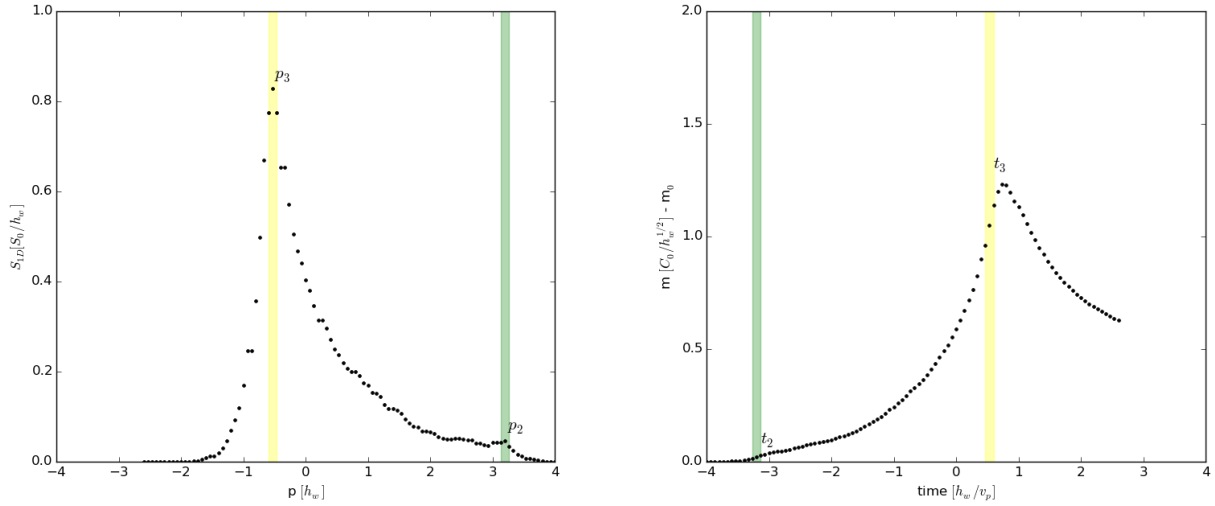


Figure 10. The one dimensional profile obtained from the numerical integration along the ordonata axis of the source image (figure 9) is presented in the left subplot. The corresponding lightcurve associated to the 1D profile is presented in the right subplot. The points p_2 and p_3 mark the start and end of the equivalent dark disk and are associated to the moments of their overlap with the caustic: t_2 and t_3 .

outer regions surrounding the luminous parts of the image have nonzero flux and thus are more extended than the simplified source model.

5 MICROLENSING CODE AND MAGNIFICATION MAPS

For the numerical computations of lightcurves for the models a and b, the microlensing code by Joachim Wambsgans was used, which is described in Wambsgans et al. (1999). This code is based on the hierachical tree technique to calculate the gravitational effect of the lensing masses. The underlying idea is that a microlensing situation can be separated into three

planes, the observer, the lens plane and the source plane (assuming the thin lens approximation to be valid). The actual effect, namely the distortion of lightrays emitted from a distant source, on the way to the observer, is numerically computed by treating this situation from the opposite side: lightrays are shot backward from the observer to lens plane, where they become deflected according to the angle, which is given by the 2-dim. mass distribution in the lens plane.

$$\vec{\alpha}_i = \frac{4G}{c^2} \frac{D_{LS}}{D_S} \sum_{j=1}^n M_j \frac{\vec{r}_{ij}}{r_{ij}^2} \quad (36)$$

For the computation of the individual deflection angles the tree idea is used. This means that the positions of all lensing masses are sorted into a 2-dimensional grid (in the lens plane). This grid is subdivided into 4 smaller squares until every cell contains only one mass. For the actual calculations of the deflection angle not every mass gravitational influence is treated equally. Instead it is made use of the fact that the influence of lenses on the considered lightray falls off with r^{-1} from the point where the ray hits the lens plane. Hence masses situated at higher distances, can be grouped together in the calculation of their gravitational potential, by multipole moments. This way the amount of computation time is reduced.

When the deflection angles are determined, the deflected lightrays are traced to the source plane and a magnification map is created by counting the number of rays which hit each of its pixels. This is the inverse of what would happen in a real observation: here an observer on earth would detect light emitted by several sources with her/his telescope. Each of these sources emits lightrays which are subject to the deflection by the intervening gravitational potential of the lensing mass. However only a fraction of those will end in the observers telescope on earth. Interesting for the analysis are hence those lightrays which are originating by the source of interest and further the subset of these which actually converge at the location of the observer. So instead of calculating the trajectories of lightrays emitted by the source in all directions and then succeedingly pick out the ones which end in the telescope of the observer, the computational effort can be restricted to these lightrays of interest in the first place. This is done by treating the problem from the opposite direction, namely by using the observers location as starting point and then shooting the lightrays backwards till they hit the source plane. The result is a pixel map of the number of lightrays which arrive at the source plane. This intermediate result is denoted as the magnification map. It characterizes the information about the mass distribution in the lens plane and its effect on lightrays, and projects this information onto the source plane.

Once the map is created, the lightcurve can be obtained by specifying the transition path of the source within the map. The code thereby convolves the function describing the shape of the source with the magnification pattern of the map for each time step (see equation 6). Note that in the most observational cases in microlensing, both lens and source are moving and further that the lens configuration, and with it the magnification pattern, is changing with time. While the first subtlety is taken care of by a coordinate transformation in this analysis, for the second one the lens configuration is assumed to be constant in time.

For the model a it was desirable to work with a caustic geometry as simple as possible. Therefore only two equal point like masses were used as lenses, to produce the magnification map depicted in figure 1. For a description of the parameter set which characterizes the map see (reference). The magnification maps calculated by the microlensing code are in units of Einstein radii, hence they are principally scale free. Physical scale is introduced to them by multiplying the pixels by the correct distance factor. The Einstein angle is given by

$$\theta_E = \sqrt{\frac{4GM}{c^2} \frac{D_{LS}}{D_S D_L}} \quad (37)$$

and therefore depends on the four parameters M, D_S, D_L, D_{LS} . For the cosmological application or quasar lensing D_L is of order 100 Mps to Gpc and D_S of order Gpc.

The scale of the magnification map can be converted into a physical length by multiplying it by a factor of $\sqrt{\frac{D_{LS}}{D_S D_L}}$.

For the next step, the computation of the actual lightcurve, the code was modified to also allow for crescent shaped images specified through the parameter set R_p, R_n, a, b . Here R_p denotes the outer radius of the crescent and R_n the inner one. The orientation of the source image with respect to the magnification map is specified by the parameters a and b as the shift of the center of the inner disk from the center of the outer disk in x - and y -direction respectively. In the original version of the code, gaussian and disk shaped images were already implemented. Those are completely characterized by the single parameter R_p . The values of the parameters are specified in pixel units corresponding to the magnification map. Further one needs to specify the start and end point coordinates of the path, which the center of the source image follows through the magnification map (see the depiction in figure 1). Hence the points along this path are specified through the number of timesteps for which the computation of the brightness is to be carried out. Those points correspond to the actual measurement of the brightness of an object in the observational case. For each timestep the two-dimensional convolution of equation 6 is carried out numerically for the position of the source on the magnification map.

For the purpose of this analysis it was desirable to mimic the analytical behavior of a simple fold as much as possible, for

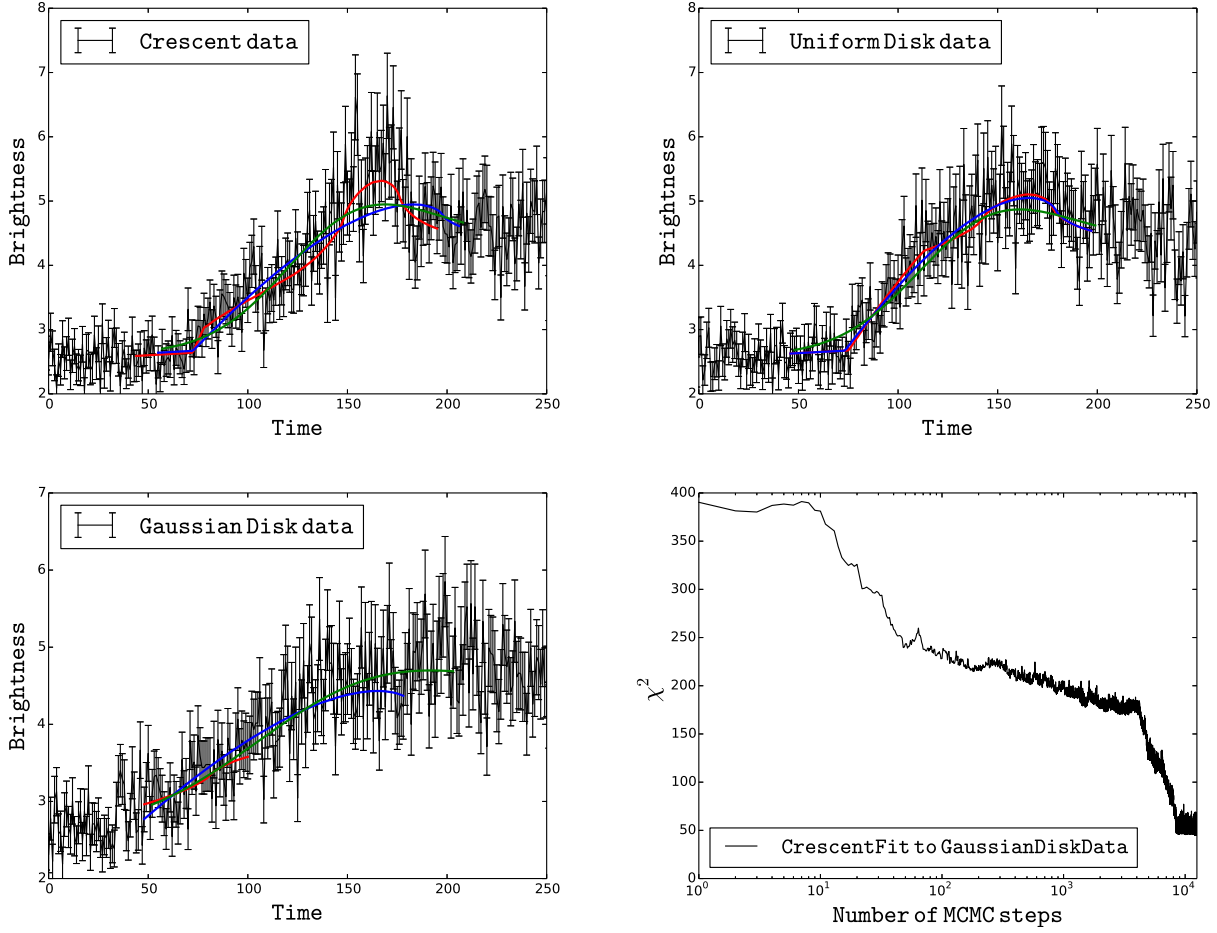


Figure 11. Three different mock datasets (in black) – crescent, uniform-disk and Gaussian disk (in reading order). In each panel showing the best fit for each of the three models - crescent (red), uniform-disk (blue) and Gaussian disk (green). Bottom-right panel shows the χ^2 of each step of the full MCMC for CG case (Gaussian disk data fitted with crescent source model)

comparing the numerical result with the analytical one, therefore the path of the source was chosen, so that it intersects the border of the caustic perpendicularly, and on a point where the border is almost straight.

6 MODEL FITTING AND LIKELIHOOD ANALYSIS

In this section, we attempt to mock three datasets, each for crescent, uniform-disk and Gaussian disk case for a given fiducial parameters and contaminate it with systematic and random noise, and fit & recover the model parameters. Broadly we have 9 cases to discuss, we name these nine cases as different permutations (couplet) of three letters C, D and G for Crescent, Uniform-Disk and Gaussian Disk case respectively. The first letter of the couplet represents the fit model and the second represents the dataset. For example, CG represents the case where we fit Gaussian disk data to a crescent model. Similarly, DC represents the case when crescent data is being fit with uniform-disk model. We explored the parameter space and carried out a likelihood analysis on all three parameter sets using Markov-chain Monte-Carlo (MCMC).

6.1 Mock datasets and model parameters

The datasets for each source model is in the form of light curves, the brightness of the source observed at different time. Figure 11 shows the three datasets. These datasets are generated using the magnification map shown in figure 1 if the source of the respective model moves from point C to B. The data assumed was very ideal, including 250 different data points at regular interval of time. We added Gaussian random noise to this dataset of width 10% of the brightness at the respective time, which makes the signal to noise of about ~ 150 . After adding random noise, the three datasets are looking highly contaminated and no clear intuitive behaviour of fit can be seen.

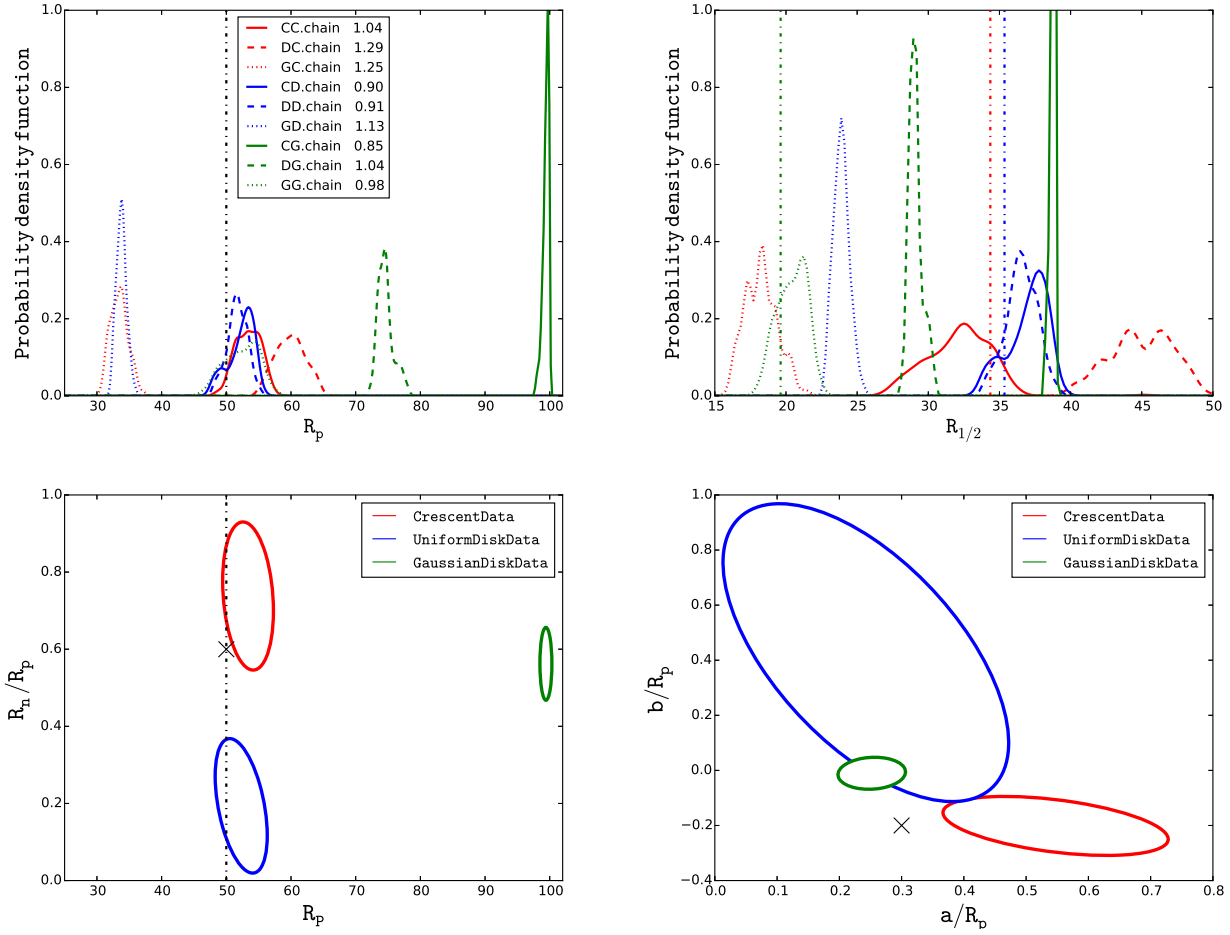


Figure 12. Top panels showing the 1D probability density function for size of the source, R_p (left), and half light radius of the source, $R_{1/2}$ (right). Same color represents the same dataset whereas same line style correspond to same model fit. In the legend showing the reduced χ^2 of the best fit in each case. Bottom two panels showing the 2σ contours (or error ellipses) of the crescent model when fitting with the three different datasets.

The fiducial model assumed to generate these mock datasets are:

$$[R_p, R_n, a, b] = [50.0, 30.0, 15.0, 10.0] \quad \text{for Crescent model,} \quad (38)$$

where, R_p and R_n are the radius of outer and inner circles of the crescent respectively and a and b are the coordinates of the inner circle center with center of outer circle as the origin.

$$R_p = 50.0 \quad \text{for Uniform disc model} \quad (39)$$

$$R_p = 50.0 \quad \text{for Gaussian disk model} \quad (40)$$

where, R_p being the size of the uniform disc and Gaussian disc source model. We also have some nuisance parameters in all these cases: the beginning of the event (I), the end of the event (E), normalisation of the lightcurve (N). We marginalised over all these nuisance parameters. When we kept these three nuisance parameters free to vary in MCMC, it adapts to the amount of data for which the maximum likelihood is most optimal to find out. We talk more about this adaptation in the next section. Secondly, We try to fit these datasets for a crossing of the source from a different caustic, in this case, from point A to B in figure 1. This adds a natural systematic in the dataset and the data is no more ideal. With these three characteristics – random noise, systematic noise and nuisance parameters – we make the dataset very general and highly contaminated to mock the real observations.

The aim of this exercise was to explore the degeneracies in various model parameters and recover the correct fiducial

model assumed from a highly contaminated dataset. Also, if it is possible that one can simply distinguish between circularly symmetric and asymmetric sources or uniform and Gaussian sources on the basis of maximum likelihoods.

6.2 Fitting with crescent model

The main results of the MCMC are shown in figure 12. In the top row, we show the nine probability density function of recovered size of the source (R_p) and its half light radius ($R_{1/2}$) (left and right respectively). The legend of top-left panel has information about the datasets, fitting model and best fit also applicable to top-right panel for $R_{1/2}$. The name of the legend has the same convention as explained in the previous section. The number accompanying the name of the legend is the best fit reduced χ^2 . We follow the convention of red, blue and green color for crescent, uniform disc and Gaussian disk datasets respectively whereas the fitting model is represented by different kind of curves: solid, dashed and dot-dashed respectively.

First we explored the parameter space for crescent source model and run its likelihood exploration for three different datasets. Here we have four interesting parameters as given by equation 38 and we marginalise over all other nuisance parameters. Three solid curves in top row of figure 12 represents the resulting likelihood of R_p , the overall size of the crescent source fitted with three different datasets. We also show results for half light radius $R_{1/2}$.

(i) Crescent data: This is the true case for crescent model fitting. The red solid line represents this case in upper panels of figure 12 as 1D probability density function marginalised over all other parameters. The true value of R_p can be recovered within 2σ level with an accuracy up to 10%. Also the best fit to the data is shown in red line in upper-left panel of figure 11. It is a very good fit which also represents a reduced χ^2 close to unity (1.04). The orange contour in the lower panels of figure 12 showing the 2D marginalised error ellipses. There is a certain degeneracy in $R_{1/2}$ and R_n/R_p parameters but all the values are well recovered.

(ii) Uniform disk data: In this case, we tried to fit crescent model to disk data. The solid blue line in top row panels and cyan contours in bottom row panel represent this case. The best fit reduced χ^2 (0.90) is better than the previous case as the data is generated by one parameter only and fitting with four parameter that can also model the noise. This can also be seen in the best fit to the data, figure 11 red line in top-right panel, where the curve seems to fit the noise as well. The maximum likelihood (and also average likelihood) is achieved close to $R_n = 0$, as already mentioned, this is intuitive as well. The other parameters, a and b are quite arbitrary and highly uncertain.

(iii) Gaussian disk data: In this case, Gaussian disk data is fitted with crescent model. The solid green line in top row panels and green contours in bottom row panels of figure 12 represent this case. By looking at figure 12, it can be seen that all the parameters can be constrained really well, even the best fit χ^2 is much better than other two cases (0.85) which also shows a bit of over-fitting problem. However, this is misleading. The reason for these strong constraints is that the full data is not at all fitted, in this case the nuisance parameters are rejecting most of the data during the progress of MCMC. This can be seen in figure 11 bottom-left panel in red line, where the best fit model is fitted only in very small range of data, even before the actual incidence happened. In other words, MCMC is unable to converge in this case and the only way to achieve better likelihood is to reject data points. This can be seen in bottom-left panel of figure 11. The χ^2 keep on reducing through the span of MCMC chain and not saturating anywhere.

Therefore we can conclude that by fitting with crescent source model, one can recover the parameters very well if the dataset is generated by crescent source model. The uniform disk source model can also be recovered very well for the overall shape of the disk, as the latter is the special case of the former, but other parameters like a and b are arbitrary and $R_n \sim 0$. No convergence can be achieved for data generated by Gaussian disk model.

Please notice that in top row of figure 12, the height of the peaks does not represents the likelihood, it is just ensuring that the area under the curve is unity. The likelihood can be estimated from the number in the legend which is the best fit χ^2 .

In the bottom rows we show three contours, for three different datasets (same color convention) fitted with crescent parameters only because this is the only case with more than one relevant parameter. Note that we plotted the 2D ellipses with principal component analysis of the MCMC and this is the reason they are perfect ellipses and not arbitrary shape.

6.3 Fitting with uniform disc model

In this case, we have only one interesting parameter to fit, the outer radius of the uniform disc with uniform intensity. When fitting with the true case, the uniform disk data itself (dashed blue line in upper panels of figure 12), the best fit χ^2 is very good (0.91) and also it recovers the true value of $R_p = 50$. When fitting with crescent data (dashed red line), the maximum likelihood shifts towards higher values of R_p as compared to the fiducial value. This is justified and intuitive as $R_n \sim 0$. Also the best fit reduced χ^2 is 1.29 which is much worse than the true case. However, when fitting with Gaussian disk data (dashed green line), the best fit reduced χ^2 is still very low but still worse than the true case. However, it can be seen in figure 11 (blue line bottom-left panel) that in this case also many points are rejected in order to gain better likelihood.

Therefore we conclude here that looking at the maximum likelihood one can identify the true dataset and also recover the true values of the parameters.

6.4 Fitting with Gaussian disc model

In the last case, we fit Gaussian disc model to the three datasets (dot-dashed curves in top panels of figure 12). In this case, when fitted with the true case, Gaussian disc dataset, the true parameters can be recovered at the correct value and also the best fit reduced χ^2 is close to unity (0.98). In all other cases the maximum likelihood is much worse and also the recovered values of R_p are many σ away.

Hence, in this case also by looking at the maximum likelihood true case can be identified and parameters can be restored correctly.

6.5 Conclusions and interpretations

The main results of this work is given in figure 12 and described in the previous section. Here we try to interpret those results and conclude the take away message.

Lets assume that an ideal telescope observes a quasar for a long time and we get the lightcurve and one can clearly see the event of caustic crossing in the light curve. Now one wants to extract the true shape of the source. To comment more specifically, lets assume three cases when the true shape of the source is: crescent, uniform disc or Gaussian disc:

(i) Crescent shape source: if one tries to fit this curve with crescent model, the maximum likelihood will be good and one can recover the true parameters with good precision. In the other two cases, the maximum likelihood will be bad. Hence this shape can be recovered very well by trusting the maximum likelihood analysis.

(ii) Uniform disc shape source: if one tries to fit this curve with Gaussian disk model, the likelihood will be very little to disprove it, however, the other two models are indistinguishable with nearly the same likelihood. At this point it does not matter as one can obtain the true result from both uniform disk and crescent model.

(iii) Gaussian disc shape source: if one tries to fit this curve with uniform disk model or crescent model, again likelihood will discard this choice. Again the maximum likelihood analysis will point towards the best fitted true model.

Therefor, we conclude that maximum likelihood analysis can be well trusted in order to recover true shape and recovering the corresponding parameters. This will provide the accurate recovery of the model parameters, however, for more precise recovery, one rely on precise measurements of the lightcurve.

7 DISCUSSION

[Mihai's contribution]

In the current paper we simulate and study the resulting microlensing lightcurves of geometric crescent-shaped sources and compare them with the microlensing lightcurves of other simple mathematically describable source profiles. In order to mimic the behaviour of flux of light from the source in the proximity of a fold caustic we make use of the simple approximation described in equation (5). The equation would exhaustively describe the magnification map and offer a good universal approximation for the particular microlensing regime that we consider. Namely, the shape of the caustic boundary in the proximity of the source in the respective plane can be approximated with a line due to reason that the local radius of curvature of caustic is orders of magnitude greater than the half-light radius of the studied source. In particular cases in which the previously mentioned approximation loses its validity the impact on the quality of the lightcurves is not evenly distributed. The shape of the lightcurve will be maintained. The datapoints corresponding to the source position before and during the overlapping of the caustic will be affected by smaller errors than the datapoints corresponding to later times.

The first two source profiles that we consider are the uniform disk and symmetric gaussian source. Both of them can be described by a half-light radius $r_{1/2}$ and a total unlensed light flux S_0 . With the two parameters constrained the one dimensional profiles as well as the lightcurves of the two source are completely determined, since no free parameter remains.

The previous statement does not hold for a crescent source. In the case of the crescent source there are in total five parameters: the integrated flux of the source S_0 , the radii of the bright/dark disk R_p/R_n and the displacement of the centers of the two disks on the axes perpendicular and parallel to the caustic a and b .

Two of the parameters can be reduced by expressing the results in terms of S_0 and $r_{1/2}$. The later being determinable for any set of parameters R_p, R_n and $a^2 + b^2$. Moreover, one of the displacement parameters b has no impact on the one dimensional profile of the source that results from the projection of the source image on an axis perpendicular to the caustic.

Since the one dimensional source profile that corresponds to an axis perpendicular to the caustic contains exhaustively

all the information regarding the source that can be revealed by the lightcurve, the value of the parameter b does not effect the shape of the lightcurve.

Nevertheless the b parameter is relevant to the calculation of $r_{1/2}$. It's qualitative effect is to decrease the value of the half-light radius when the absolute value of the parameter is increased. With two parameters constrained and another irrelevant to the shape of the lightcurve, two free parameters remain R_n and a . Figure 4 reveals that the lightcurve of a crescent source has more visible features than the other two light-curves corresponding to the disc and gaussian shape. The parameters R_n and a have strong influences on the shape of the microlensed lightcurve, as can be seen in figures 5, 6 and 7. Moreover, the one dimensional source profile corresponding to the direction perpendicular to the caustic reveal four characteristic points. The overlap of each of these points with the caustic leaves visible features on the lightcurve at the corresponding instances of time. In timely order the instances correspond to the start of the overlap between the caustic and the bright disk, the start of the overlap between the caustic and the dark disk, the end of the overlap between the caustic and dark disk and finally the end of the overlap between the caustic and the bright disk.

With the different source profiles and their corresponding lightcurves studied we can change our point of view of the system to that of an observer. The observer would basically detect only the lightcurve of such as source. As described in section (Lightcurve of a crescent source) the timing of the onset and offset of the previously described periods can be used to estimate the values of the radii and one of the displacement parameters when assuming a geometric crescent, the halfwidths and one displacement parameters when assuming a constant brightness elliptical crescent and the halfwidth of the dark ellipse when assuming an elliptical gaussian crescent. All quantities can be estimated in terms of the relative velocity of the source in a direction perpendicular to the caustic.

The previously mentioned abstract parameters can be related to physical quantities specific to the central region of a quasar. Thus the luminous region would correspond to the bright accretion disc that surrounds the black hole. The later's gravity would cause a shadow in the bright region limited by the extent of the event horizon of the black hole. Therefore the radius of the bright disk would provide an estimate of the size of the accretion disk and the radius of the dark disk would provide and estimate of the Schwarzschild radius of the black hole. Moreover a value of the Schwarzschild radius can be used to estimate the mass of the black hole $M \approx \frac{\Delta t_{dark} v_p c^2}{2G}$. In the previous expression the Δt_{dark} denotes the period of overlap between the black hole shadow and fold caustic. v_p denotes the component of the relative velocity of the source and fold which is perpendicular to the caustic. Furthermore, a simulated image of M87 presented in (Dexter et al. 2012) (figure 9) has been microlensed. On the resulting lightcurve the instances corresponding to the start and end of the black hole shadow and caustic overlap were distinguishable as can be seen in figure 10.

The parameters whose values cannot be determined due to the loss of information from the directions parallel to the caustic could be obtained in the eventuality in which the same source crosses multiple caustics that are not parallel. Multiple crossing of caustics can reveal details of the one dimensional flux profile corresponding to multiple distinct directions which would allow the reconstruction of the two dimensional profile analogous to the process through which an image of a CT scan is obtained.

In case of a high quality lightcurve with insignificant noise and measurement errors, the parameters can be obtained by simply identifying the characteristic instances of time without making use of the actual values of the magnification map. If the effect of the errors and the noise distorts the magnification time function enough so that the characteristic points are not identifiable with the characteristic periods still visible, the boundaries of the periods can be roughly estimated. To study if good estimates of the parameters can still be obtained when datapoints are strongly affected by the noise we propose

[Irshad's contribution]

This work presents a toy model to put useful constraints on the interior structure of quasars, particularly the environment geometry of the event horizon. To carry out this analysis on real data, one needs two situations: First, a quasar which can be observed with a reasonably good telescope with high signal to noise (~ 150) and second, a caustic crossing event of the quasar. These events are not rare, however, to get an isolated caustic crossing might be. As the size of the source is negligible as compared to big caustic structures in the sky, even the single fold caustic crossing is not that rare.

In this toy analysis, we used very ideal data, which might not be the case with real source but we contaminated it to match a reasonable signal to noise.

The main emphasis of this work was the crescent model parameters, which we show can be well recovered by the maximum likelihood analysis, apart from highly degenerate a and b parameters. The reason of this degeneracy is also very intuitive, if one integrates parallel to the caustic to get the integrated 1D brightness profile, so if the motion of the source is either parallel or perpendicular to the caustic, one of the two parameters (a and b) is indistinguishable and in case of angled motion of the source, these two are highly degenerate. This degeneracy can be broken if multiple crossing events of the same quasar is available. So for example, one can use the first crossing to estimate the likelihood of the four parameters and use them as priors in the second crossing and so on. In this way, one can accurately and precisely recover all four parameters. Using

our toy analysis we conclude that it is feasible, in practice, to recover 2D shape of the source using a microlensing event and distinguish between symmetric and asymmetric sources.

[Contributions from authors]

Prasenjit Saha provided the original idea and plan for the research project as well as multiple contributions to the analysis. Mihai Tomozeiu simulated and studied the ideal behaviour of the microlensing lightcurves for the different source profiles discussed. Joachim Wambsganss provided the numerical code used by Manuel Rabold to create the magnification map and corresponding lightcurves used in the MCMC analysis, analysis that was performed by Irshad Mohammed in the last part of the presented work.

REFERENCES

- Begelman M. C., Blandford R. D., Rees M. J., 1984, *Reviews of Modern Physics*, 56, 255
Blandford R., Narayan R., 1986, *ApJ*, 310, 568
Broderick A. E., Fish V. L., Doeleman S. S., Loeb A., 2011, *ApJ*, 738, 38
Dexter J., Agol E., Fragile P. C., McKinney J. C., 2010, *ApJ*, 717, 1092
Dexter J., McKinney J. C., Agol E., 2012, *MNRAS*, 421, 1517
Doeleman S., 2008, *Journal of Physics Conference Series*, 131, 012055
Doeleman S. S. et al., 2012, *Science*, 338, 355
Doeleman S. S. et al., 2008, *nature*, 455, 78
Gaudi B. S., Petters A. O., 2002a, *ApJ*, 574, 970
Gaudi B. S., Petters A. O., 2002b, *ApJ*, 580, 468
Gott, III J. R., 1981, *ApJ*, 243, 140
Kamruddin A. B., Dexter J., 2013, *MNRAS*, 434, 765
Lynden-Bell D., 1969, *nature*, 223, 690
McKinney J. C., Blandford R. D., 2009, *MNRAS*, 394, L126
Mościbrodzka M., Gammie C. F., Dolence J. C., Shiokawa H., Leung P. K., 2009, *ApJ*, 706, 497
Pâris I. et al., 2014, *A&A*, 563, A54
Reid M. J., 1993, *ARAA*, 31, 345
Ricarte A., Dexter J., 2015, *MNRAS*, 446, 1973
Salpeter E. E., 1964, *ApJ*, 140, 796
Schneider P., Weiss A., 1986, in *Bulletin of the American Astronomical Society*, Vol. 18, *Bulletin of the American Astronomical Society*, p. 907
Schneider P., Weiss A., 1992, *A&A*, 260, 1
Wambsganss J., 1990, 360, 186
Wambsganss J., 2001, *PASA*, 18, 207
Wambsganss J., Brunner H., Schindler S., Falco E., 1999, *A&A*, 346, L5
Zel'dovich Y. B., Novikov I. D., 1964, *Soviet Physics Doklady*, 9, 246